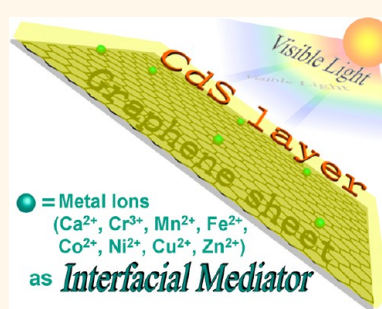


Toward Improving the Graphene–Semiconductor Composite Photoactivity *via* the Addition of Metal Ions as Generic Interfacial Mediator

Nan Zhang,^{†,‡} Min-Quan Yang,^{†,‡} Zi-Rong Tang,[‡] and Yi-Jun Xu^{†,‡,*}

[†]State Key Laboratory Breeding Base of Photocatalysis, College of Chemistry and Chemical Engineering, Fuzhou University, Fuzhou 350002, People's Republic of China and [‡]College of Chemistry and Chemical Engineering, New Campus, Fuzhou University, Fuzhou 350108, People's Republic of China

ABSTRACT We report a simple and general approach to improve the transfer efficiency of photogenerated charge carriers across the interface between graphene (GR) and semiconductor CdS by introducing a small amount of metal ions (Ca^{2+} , Cr^{3+} , Mn^{2+} , Fe^{2+} , Co^{2+} , Ni^{2+} , Cu^{2+} , and Zn^{2+}) as “mediator” into their interfacial layer matrix, while the intimate interfacial contact between GR and CdS is maintained. This simple strategy can not only significantly improve the visible-light-driven photoactivity of GR–CdS semiconductor composites for targeting selective photoredox reaction, including aerobic oxidation of alcohol and anaerobic reduction of nitro compound, but also drive a balance between the positive effect of GR on retarding the recombination of electron–hole pairs photogenerated from semiconductor and the negative “shielding effect” of GR resulting from the high weight addition of GR. Our current work highlights that the significant issue on improving the photoactivity of GR–semiconductor composites *via* strengthening interfacial contact is not just a simple issue of tighter connection between GR and the semiconductor, but it is also the optimization of the atomic charge carrier transfer pathway across the interface between GR and the semiconductor.



KEYWORDS: graphene · semiconductor · mediator · interfacial composition engineering · selective photoredox

Recent years have witnessed a flourish of interest in the use of graphene (GR) as cocatalyst to construct various GR–semiconductor composites toward enhancing the photocatalytic performance of semiconductors for solar energy conversion.^{1–12} The unique 2D structure and excellent electronic properties of GR endow this cocatalyst with the prominent capability to accept/transport electrons photogenerated from band gap photoexcitation of semiconductors upon light irradiation.^{1–32} Therefore, the optimization and manipulation of charge carrier transfer processes across the interface between GR and semiconductors is a critically key and broad theme toward improving the photocatalytic efficiency of such GR–semiconductor composite-based artificial photosynthesis processes.^{3–7,19–28} To date, the intimate interfacial contact between GR and semiconductors has been recognized to be a key factor for sufficient utilization of electron conductivity of GR, thus improving

the photoactivity of GR–semiconductor composites more efficiently.^{1–32} However, this significant issue on improving the photoactivity of GR–semiconductor composites *via* strengthening interfacial contact is not just a simple issue of tighter connection between GR and semiconductors, but it is also the optimization of interfacial atomic charge carrier transfer pathways resulting from the rational synergy interaction between respective individual components integrated in GR–semiconductor composites.⁶ In this sense, it is of crucial importance to propose conceptual strategies to boost the photogenerated charge carrier lifetime and transfer efficiency across the interface between GR and semiconductors. Unfortunately, to the best of our knowledge, it has still remained totally unclear for the study in this significant aspect.^{1–32}

On the other hand, the “shielding effect” induced by the high weight addition of GR cocatalyst, due to its opacity which weakens the light irradiation depth through the

* Address correspondence to yjxu@fzu.edu.cn.

Received for review October 8, 2013 and accepted December 4, 2013.

Published online December 04, 2013
10.1021/nn405242t

© 2013 American Chemical Society

GR–semiconductor composites and reaction medium, unavoidably restricts the efficiency of GR in promoting the photoactivity of GR–semiconductor composites.^{2–4,6,7,10,13,14,17–20,27,28,30–32} This intrinsic negative effect leads to the fact that, in order to achieve an optimal photoactivity enhancement for GR–semiconductor composites, the weight addition ratio of GR into the semiconductor matrix is generally no more than 5%, although the greater addition ratio of GR is able to positively inhibit the recombination of electron–hole pairs photogenerated from the semiconductor.^{1–4,6–10,13–21,26–32} Such a double-edged sword role of GR also limits the net efficiency of promoting the overall photoactivity of GR–semiconductor composites. These aforementioned two issues could be regarded as two typical bottlenecks that restrict the degree of improving the photoactivity and more efficient fabrication of GR–semiconductor composites.^{1–32}

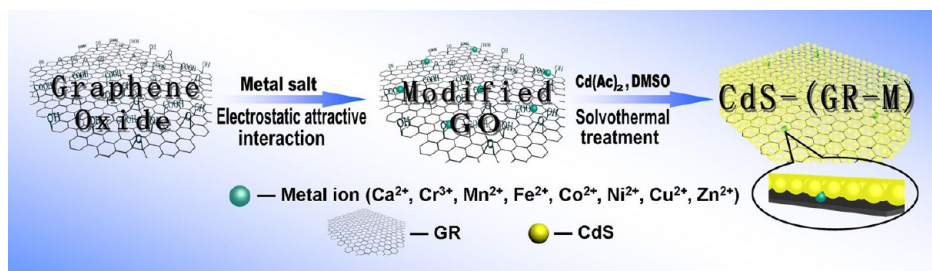
Herein, we report a facile, conceptual, and general strategy *via* interfacial composition engineering, that is, introducing a small amount of metal ions (Ca^{2+} , Cr^{3+} , Mn^{2+} , Fe^{2+} , Co^{2+} , Ni^{2+} , Cu^{2+} , and Zn^{2+}) into the interfacial layer matrix between GR and the semiconductor, to significantly improve the visible light photoactivity of GR–semiconductor composites, while the intimate interfacial contact between GR and the semiconductor is still retained. The results reveal that this simple approach can optimize the transfer pathway of photogenerated charge carriers across the interface between GR and the semiconductor and improve the lifetime and transfer of charge carriers more effectively under visible light irradiation. In addition, it can partially offset the shielding effect of GR due to a high weight addition of GR. Consequently, the photoactivity of GR–semiconductor composites is remarkably enhanced, as evidenced by the aerobic selective oxidation of alcohol and anaerobic reduction of nitro compound under visible light irradiation. This work highlights that the optimization of interfacial composition between GR and semiconductors (*e.g.*, introducing metal ions or other heteroatoms as interfacial mediator) could offer a conceptually new strategy to boost the lifetime and transfer efficiency of photogenerated

charge carriers across the interface between GR and semiconductors. As a result, the more efficient and smarter GR–semiconductor photocatalysts would be achieved toward various targeting applications in solar energy conversion.

RESULTS AND DISCUSSION

We choose CdS, a well-known II–VI semiconductor with suitable band gap (*ca.* 2.4 eV) corresponding well with the spectrum of sunlight, as an example to prepare a series of CdS–(GR–M) ($M = \text{Ca}^{2+}$, Cr^{3+} , Mn^{2+} , Fe^{2+} , Co^{2+} , Ni^{2+} , Cu^{2+} , and Zn^{2+}) nanocomposites with different weight addition ratios of GR *via* a simple wet chemistry process. One important reason for choosing CdS as a typical example of semiconductor is based on the fact that it has been well-established that the simple, one-step solvothermal treatment of cadmium acetate ($\text{Cd}(\text{Ac})_2$), dimethyl sulfoxide (DMSO), and graphene oxide (GO, the precursor of GR) can directly produce CdS–GR nanocomposites with excellent intimate interfacial contact.^{3,26,35} The other important reason is that, using this simple solvothermal method, the premodification of GO by anchoring a few amounts of metal ions does not have an influence on the formation of CdS on the GR sheet, and the intimate interfacial contact between CdS and GR can still be retained, which provides a basic and reasonable framework to comparatively study the effect of metal ion addition into the interfacial matrix between GR and CdS on the lifetime/transfer of photogenerated charge carriers and the photoactivity for the nanocomposites of CdS–(GR–M) and CdS–GR under visible light irradiation.

Our synthesis procedure of CdS–(GR–M) ($M = \text{Ca}^{2+}$, Cr^{3+} , Mn^{2+} , Fe^{2+} , Co^{2+} , Ni^{2+} , Cu^{2+} , and Zn^{2+}) nanocomposites is illustrated in Scheme 1. Graphene oxide (GO), fabricated by the modified Hummers method,^{2,4,26–28,30,33,34} is functionalized by the anchoring of a few amounts of metal ions at first. Such a surface modification of GO can be easily realized by the electrostatic attractive interaction between positively charged metal ions ($M = \text{Ca}^{2+}$, Cr^{3+} , Mn^{2+} , Fe^{2+} , Co^{2+} , Ni^{2+} , Cu^{2+} , and Zn^{2+}) and oxygen atoms of negatively charged oxygenated functional groups on the GO



Scheme 1. Flowchart illustrating the fabrication of CdS–(GR–M) ($M = \text{Ca}^{2+}$, Cr^{3+} , Mn^{2+} , Fe^{2+} , Co^{2+} , Ni^{2+} , Cu^{2+} , and Zn^{2+}) nanocomposites in which metal ions are introduced to the interfacial layer matrix between GR and semiconductor CdS.

surface in water (Figure S1, Supporting Information). In addition, the possible binding interaction between metal ions with defect sites on the GO sheet could also contribute to the effective anchoring of metal ions onto the GO sheet. The X-ray photoelectron spectra (XPS) analysis is used to determine the valence state and weight content of metal in the metal-ion-modified GO (Figures S2–S9, Supporting Information), such as GO–M. As summarized in Table S1 (Supporting Information), the valence state of metal in GO–M is the same as that of the precursor metal salts, suggesting that the oxygenated functional groups on the GO surface do not reduce these positively charged metal ions ($M = \text{Ca}^{2+}$, Cr^{3+} , Mn^{2+} , Fe^{2+} , Co^{2+} , Ni^{2+} , Cu^{2+} , and Zn^{2+}) to metallic ones during the present process for GO modification. The binding of metal ions and oxygen atoms on the GO surface can also be reflected by the Fourier transform infrared (FTIR) spectroscopy analysis on these GO–M samples (Figures S10, Supporting Information). The weight contents of metal ions (M) in GO–M are determined to be *ca.* 2.44, 2.07, 2.02, 2.43, 1.82, 1.12, 1.30, and 3.74%, corresponding to GO–Ca, GO–Cr, GO–Mn, GO–Fe, GO–Co, GO–Ni, GO–Cu, and GO–Zn, respectively, based on the XPS quantification analysis (Table S1, Supporting Information).

In particular, it should be stressed that, during this step of modification of GO by metal ion anchoring, sufficient centrifugation and washing treatments are necessary to completely remove the dissolved chloride and metal ions in solution or weakly physisorbed metal ions on GO. This will (i) exclude the detrimental effect of chloride ions on the formation of CdS resulting from the reaction of cadmium acetate ($\text{Cd}(\text{AC})_2$) and the DMSO solvent because the controlled experiment for synthesis of CdS using CdCl_2 instead of $\text{Cd}(\text{AC})_2$ as the source of cadmium of CdS shows no formation of CdS in the DMSO solvent *via* such a solvothermal treatment process, and (ii) guarantee the strong binding interaction between metal ions (Ca^{2+} , Cr^{3+} , Mn^{2+} , Fe^{2+} , Co^{2+} , Ni^{2+} , Cu^{2+} , and Zn^{2+}) and GO, which will prevent the subsequent formation of metal sulfides due to the reaction of GO–M with dimethyl sulfoxide (DMSO) during the solvothermal treatment. Then, this metal-ion-modified GO (GO–M) and cadmium acetate are dispersed into the dimethyl sulfoxide (DMSO) solvent, subjected to one-step solvothermal treatment,^{3,26,35} during which the production of CdS nanoparticles, reduction of insulating GO to electron conducting GR, and excellent intimate interfacial contact can be simultaneously achieved. As a result, the CdS–(GR–M) nanocomposites with different weight addition ratios of GR are obtained. For comparison, the CdS–GR counterparts with different weight addition ratios of GR have also been prepared through the same

preparation procedure except the addition of GO instead of metal-ion-modified GO (GO–M).^{3,26,35}

To rule out the possibility of formation of metal sulfides resulting from the reaction of metal ions in GO–M with DMSO during the solvothermal treatment, we have performed the following controlled experiments. Similar to the modification of GO with binding of metal ions (GO–M, $M = \text{Ca}^{2+}$, Cr^{3+} , Mn^{2+} , Fe^{2+} , Co^{2+} , Ni^{2+} , Cu^{2+} , and Zn^{2+}), we have prepared the sample of GO with binding of metal ion Cd^{2+} (*i.e.*, GO–Cd) using the same preparation procedure as that of GO–M except using CdCl_2 . Then, the GO–M and GO–Cd are subjected to the same solvothermal treatment in the DMSO solvent. The as-obtained samples are then analyzed by the XRD and Raman analysis. In the XRD spectra in Figure S11 (Supporting Information), only peaks corresponding to GR can be observed for the samples of GR–M ($M = \text{Ca}^{2+}$, Cr^{3+} , Mn^{2+} , Fe^{2+} , Co^{2+} , Ni^{2+} , Cu^{2+} , and Zn^{2+}). There are no detectable diffraction peaks of metal sulfides; however, in distinct contrast, in addition to the peaks corresponding to GR for the sample of GR–Cd, two other diffraction peaks at *ca.* 26.5 and 44.0° can also be clearly observed, which are attributed to the (111) and (220) crystal planes of cubic CdS (JCPDS Card No. 10-0454). To further confirm the absence of metal sulfides for the samples of GR–M ($M = \text{Ca}^{2+}$, Cr^{3+} , Mn^{2+} , Fe^{2+} , Co^{2+} , Ni^{2+} , Cu^{2+} and Zn^{2+}), we have further done the contrast Raman spectra analysis among the samples of GR–M ($M = \text{Ca}^{2+}$, Cr^{3+} , Mn^{2+} , Fe^{2+} , Co^{2+} , Ni^{2+} , Cu^{2+} , and Zn^{2+}) and GR–Cd. It is clear to see from Figure S12 (Supporting Information) that, only for the sample of GR–Cd, the characteristic Raman shift peak of CdS is clearly observed, which is in line with the XRD spectra. However, no characteristic Raman shift peaks of metal sulfides are identified for the samples of GR–M ($M = \text{Ca}^{2+}$, Cr^{3+} , Mn^{2+} , Fe^{2+} , Co^{2+} , Ni^{2+} , Cu^{2+} , and Zn^{2+}). The XPS spectra (data not shown) also confirm the absence of sulfur for GR–M; that is, no metal sulfides are formed for GR–M. This means that, during the solvothermal treatment process of GO–M ($M = \text{Ca}^{2+}$, Cr^{3+} , Mn^{2+} , Fe^{2+} , Co^{2+} , Ni^{2+} , Cu^{2+} , and Zn^{2+}) in the DMSO solvent, only GO is reduced to GR while the binding of metal ions is strong enough, thereby inhibiting the reaction of GO–M with DMSO to produce metal sulfides. However, the case is different for the case of GO–Cd, suggesting that this simple, one-step solvothermal treatment in the DMSO solvent is exclusive for the formation of CdS instead of other metal sulfides. This consequently offers a reasonable framework to comparatively study the effect of metal ion addition into the interfacial matrix between GR and CdS on the lifetime/transfer of photogenerated charge carriers and the photoactivity for CdS–(GR–M) and CdS–GR nanocomposites under visible light irradiation.

Figure S13 (Supporting Information) shows the XRD patterns of CdS-(GR-M) and CdS-GR with different weight addition ratios of GR, which possess the analogous XRD patterns. The well-resolved broad diffraction peaks at 26.5, 44.0, and 52.1° can be indexed to the (111), (220), and (311) crystal planes of cubic CdS (JCPDS Card No. 10-0454), respectively. The estimated average crystallite sizes of CdS in CdS-(GR-M) and CdS-GR based on the Scherrer formula further indicate that all the samples of CdS-(GR-M) and CdS-GR with different weight addition ratios of GR have similar crystallite size of CdS (Table S2, Supporting Information). The optical property measurement (Figure S14, Supporting Information), using the UV-vis diffuse reflectance (DRS) spectra, shows that the samples of CdS-(GR-M) and CdS-GR feature the analogous light absorption fingerprint in the visible light region (500–800 nm); with the increased weight addition of GR, the visible light absorption of CdS-(GR-M) or CdS-GR is enhanced gradually, which can be attributed to the intrinsic background absorption of black colored GR.^{2-4,14,26-28,30-32,34} The XRD and DRS results suggest that the introduction of a few amounts of metal ions does not have a significant effect on the crystallization process of CdS particles onto the GR surface, crystal phase, and crystallite size of CdS particles that are *in situ* formed on the GR surface and on the light absorption property of the CdS-(GR-M) and CdS-GR composites. In particular, the analogous optical properties between CdS-(GR-M) and CdS-GR indicate that the metal ions are located in the interfacial layer between GR and CdS, instead of the doping of metal ions into the crystalline domain of CdS. This is in agreement with the above controlled experiment showing the strong binding of metal ions to the GO surface and thus that such a solvothermal treatment of GO-M in DMSO is not able to lead to the formation of metal sulfides besides CdS.

In the following, we have benchmarked the photoactivity comparison between CdS-(GR-M) and CdS-GR under visible light irradiation using two typical probe reactions including aerobic oxidation of alcohol and anaerobic reduction of nitro compound. It is remarkable to find the significant difference in photoactivity between the two series of samples. As shown in Figure 1A, the direct coupling of CdS with GR can improve the photoactivity of CdS moderately. The optimal weight addition ratio of GR is 5%; that is, CdS-5% GR shows the highest photoactivity. Under visible light irradiation for 2 h, the conversion for oxidation of benzyl alcohol over the optimal CdS-5% GR photocatalyst is *ca.* 34%, while over blank CdS (*i.e.*, 0% GR), the conversion of benzyl alcohol is *ca.* 26%. Therefore, it is clear that this improvement in photoactivity of CdS is fairly limited. However, after the introduction of a few amounts of metal ions ($M = \text{Ca}^{2+}, \text{Cr}^{3+}, \text{Mn}^{2+}, \text{Fe}^{2+}, \text{Co}^{2+}, \text{Ni}^{2+}, \text{Cu}^{2+}, \text{and Zn}^{2+}$)

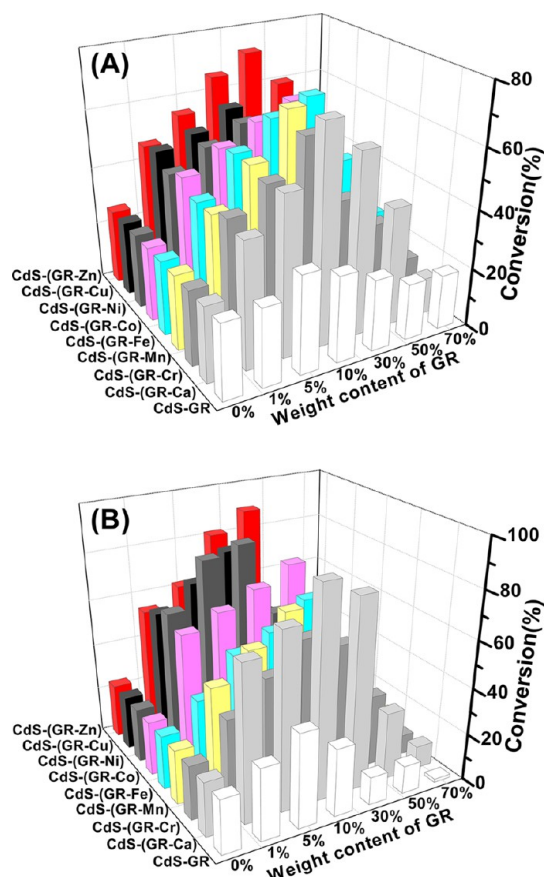


Figure 1. Photocatalytic performance of blank CdS, CdS-GR, and CdS-(GR-M) ($M = \text{Ca}^{2+}, \text{Cr}^{3+}, \text{Mn}^{2+}, \text{Fe}^{2+}, \text{Co}^{2+}, \text{Ni}^{2+}, \text{Cu}^{2+}, \text{and Zn}^{2+}$) nanocomposites with different weight addition ratios of GR for (A) photocatalytic selective oxidation of benzyl alcohol under visible light ($\lambda > 420 \text{ nm}$) for 2 h and (B) selective reduction of 4-nitroaniline under visible light irradiation ($\lambda > 420 \text{ nm}$) for 80 min.

into the interlayer matrix between GR and CdS, the photoactivity toward oxidation of benzyl alcohol is significantly improved. For example, over the optimal CdS-10% (GR-Ca) photocatalyst, the conversion of benzyl alcohol under visible light irradiation for 2 h is remarkably increased to *ca.* 73%, which is more than 2 times higher than that over the optimal CdS-5% GR. Furthermore, for the optimal CdS-(GR-M) photocatalysts, the weight addition ratio of GR is remarkably increased to 10 or 30%. This observation is quite interesting because, due to the shielding effect of GR, the optimal weight addition ratio of GR for GR-semiconductor composite photocatalysts is generally $\leq 5\%$ in order to achieve a proper synergy interaction between GR and the semiconductor, as widely reported in previous works regarding the GR-semiconductor composite photocatalysts regardless of what kind of probe reaction is taken.^{1-4,6-10,12-16,18-21,26-34} Time-online profiles for oxidation of benzyl alcohol, as displayed in Figure 2A, faithfully ensure that the optimal CdS-(GR-M) photocatalysts exhibit much

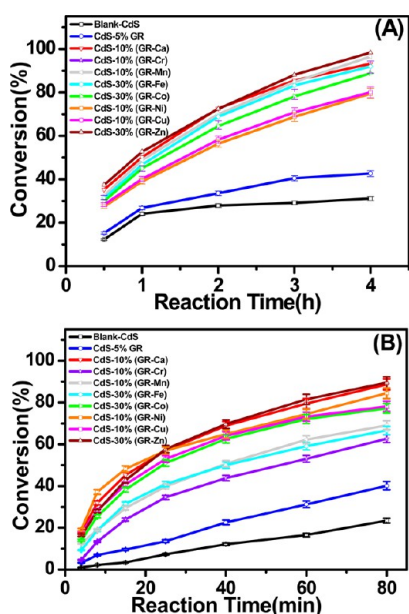


Figure 2. Time-online profiles of conversion of (A) benzyl alcohol and (B) 4-nitroaniline over blank CdS and the optimal CdS–5% GR, CdS–10% (GR–Ca), CdS–10% (GR–Cr), CdS–10% (GR–Mn), CdS–30% (GR–Fe), CdS–30% (GR–Co), CdS–10% (GR–Ni), CdS–10% (GR–Cu), and CdS–30% (GR–Zn) nanocomposites under visible light irradiation ($\lambda > 420$ nm).

higher photoactivity than both the optimal CdS–5% GR and blank CdS. In addition, over these optimal CdS–(GR–M) or CdS–GR photocatalysts, the primary product for oxidation of benzyl alcohol is benzaldehyde with a high selectivity (>95%). Controlled photoactivity test for benzyl alcohol oxidation over the GR–M ($M = \text{Ca}^{2+}$, Cr^{3+} , Mn^{2+} , Fe^{2+} , Co^{2+} , Ni^{2+} , Cu^{2+} , and Zn^{2+}) samples under visible light irradiation for 2 h shows that the as-obtained yield of benzaldehyde is generally lower than 2%, thus confirming that the primary photoactive ingredient is semiconductor CdS.

Such a similar photoactivity trend has also been observed for anaerobic selective reduction of 4-nitroaniline (4-NA), a typical nitro compound, to *p*-phenylenediamine (PPD) over CdS–GR, CdS–(GR–M), and blank CdS under visible light irradiation, as shown in Figures 1B and 2B (for further details, see Figures S15–S23 and Table S3 in the Supporting Information). The high-performance liquid chromatograph (HPLC) analysis has been used to quantify the distribution of reactant and product. The results confirm that the product is primarily dominated by PPD with a high selectivity (>95%). Furthermore, it is worth noting that the optimal CdS–(GR–M) photocatalysts for selective reduction of 4-NA are the same as those for selective oxidation of benzyl alcohol, indicating that an optimum synergistic interaction between GR–M and CdS semiconductor has been simultaneously achieved for these two different selective photocatalytic redox reactions. The above results suggest that, on one hand,

the introduction of a few amounts of metal ions into the interlayer matrix between GR and CdS can largely improve the photoactivity of CdS–GR composites and, on the other hand, counterbalance the shielding effect induced by the higher weight addition of GR. In other words, the overall net efficiency of improving the semiconductor photoactivity is remarkably enhanced due to the addition of metal ions into the interfacial layer matrix of GR and semiconductor CdS. In addition, a controlled photoactivity test for 4-NA reduction over the GR–M ($M = \text{Ca}^{2+}$, Cr^{3+} , Mn^{2+} , Fe^{2+} , Co^{2+} , Ni^{2+} , Cu^{2+} , and Zn^{2+}) samples under visible light irradiation for 2 h shows trace yield of PPD, which confirms that the primary photoactive ingredient is semiconductor CdS.

To unveil the origin accounting for the much higher photoactivity of CdS–(GR–M) than CdS–GR and the improved optimal weight addition of GR observed in CdS–(GR–M), we have then comparatively characterized the samples with optimal photoactivity by a series of joint techniques. Figure 3 shows the typical TEM images of CdS–5% GR, CdS–10% (GR–Ca), CdS–10% (GR–Cr), CdS–10% (GR–Mn), CdS–30% (GR–Fe), CdS–30% (GR–Co), CdS–10% (GR–Ni), CdS–10% (GR–Cu), and CdS–30% (GR–Zn), from which it can be seen that all of these samples feature the analogous microscopic structural morphology. The CdS nanoparticles uniformly carpet the GR surface, forming an intimate interfacial contact between CdS and GR. To further glean the microscopic information, we have taken CdS–10% (GR–Ca) as an example for the HRTEM analysis. As shown in Figure 4B, the GR layer can be clearly seen in the edge area of the sample. Due to the shielding of the CdS layer, we cannot distinguish metal ions from the HRTEM analysis. However, the presence of tiny amounts Ca metal ion is confirmed by the energy-dispersive X-ray (EDX) analysis (panels C and D in Figure 4). For clarity, the partially enlarged EDX results from panels D and E are referenced as panels C-1, C-2, D-1, and D-2, from which the signals of element Ca are clearly identified. The TEM results suggest that the difference of structure/morphology between CdS–GR and CdS–(GR–M) cannot be the primary reason leading to the significant photoactivity enhancement of CdS–(GR–M) as compared to CdS–GR.

Since the addition of metal ions does not affect the coupling structure/morphology between CdS and the GR sheet, we infer that the role of metal ions may help optimize the photogenerated charge carrier pathway or efficiency across the interface between CdS and GR. In other words, under visible light irradiation, the electron–hole pairs are generated from semiconductor CdS due to its band gap photoexcitation. Because of the excellent electron conductivity of the GR sheet, the GR platform is able to accept and shuttle the photogenerated electrons from CdS.^{1–32} The presence of metal ions in the interlayer matrix between CdS and

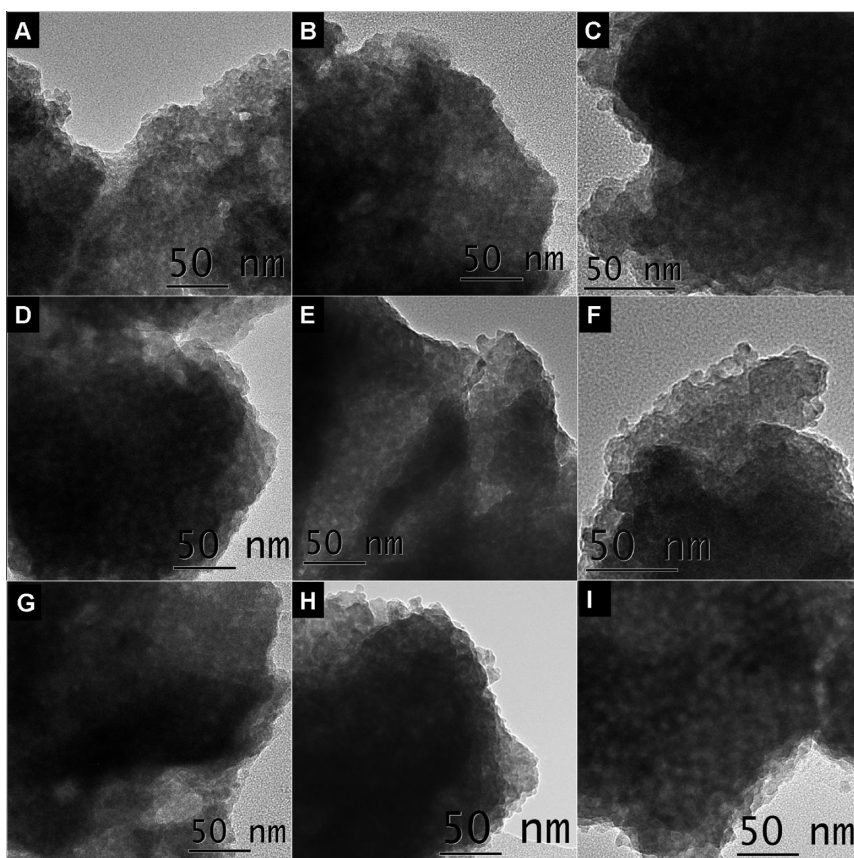


Figure 3. TEM images of the optimal (A) CdS-5% GR, (B) CdS-10% (GR-Ca), (C) CdS-10% (GR-Cr), (D) CdS-10% (GR-Mn), (E) CdS-30% (GR-Fe), (F) CdS-30% (GR-Co), (G) CdS-10% (GR-Ni), (H) CdS-10% (GR-Cu), and (I) CdS-30% (GR-Zn) nanocomposites.

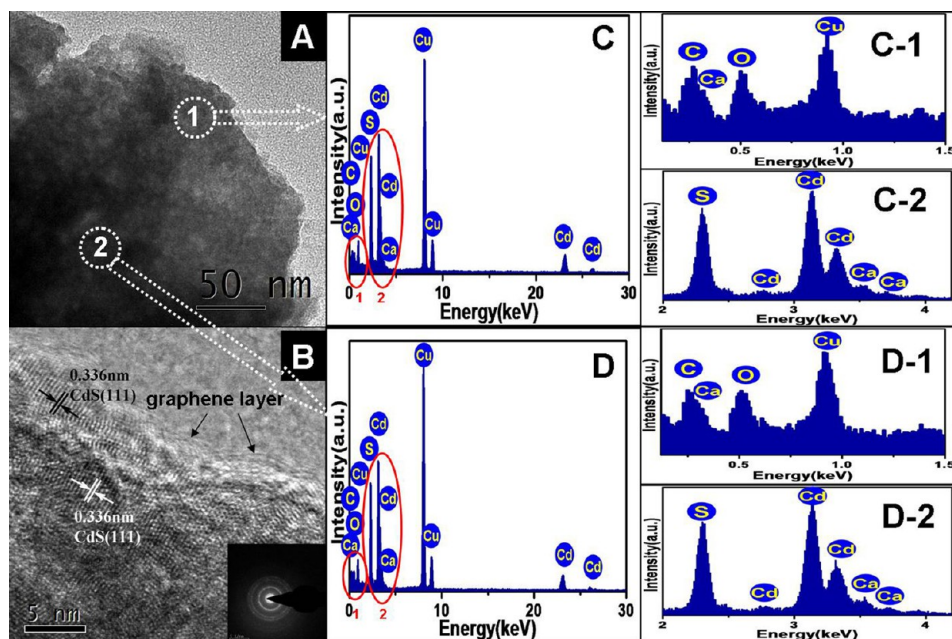


Figure 4. TEM (A), HRTEM (B), and EDX (C, D) of the CdS-10% (GR-Ca) nanocomposite; for better clarity, the local regions of the EDX spectra indicated by the red ovals in panels C and D are enlarged as C-1, C-2, D-1, and D-2; the inset of panel B is the image of the SAED pattern.

GR could optimize the photogenerated electron transfer pathway from semiconductor CdS to the electron

conductive GR, by which the lifetime of charge carriers (electron-hole pairs) is prolonged. This in turn would

contribute to the photoactivity improvement of the CdS–GR nanocomposites because, according to the principle of semiconductor-based photocatalysis, the lifetime of photogenerated charge carriers is a key factor affecting the activity of a specific photocatalyst.^{1–32,36,37} Our inference is verified by the following photoluminescence (PL) analysis. It is well-known that the PL spectra are widely used as an effective technique to study surface processes involving the fate of charge carriers photoexcited from semiconductors.^{15,19,20,27,38} As shown in Figure 5, the addition of GR into the semiconductor CdS matrix can decrease the PL intensity. The higher addition of GR will result in a higher quenching degree of PL intensity, suggesting the more efficient inhibition of electron–hole pair recombination.^{15,19,20,27,38} However, as mentioned above, the higher addition of GR simultaneously brings the negative shielding effect, which will lower the photoactivity.^{2–4,6,7,13,14,18–21,26–32} Thus, the weight addition ratios of GR for achieving an optimal photoactivity is generally low ($\leq 5\%$), in order to balance the positive effect of GR on retarding the recombination of electron–hole pairs photogenerated from semiconductors and the negative shielding effect of GR.^{2–4,6,7,13,14,18–21,26–32}

However, when a tiny amount of metal ions is introduced into the interlayer matrix between CdS and GR, it is quite interesting to observe the more efficient quenching of PL intensity for CdS–(GR–M) than that for CdS–GR. For example, the PL intensity for the optimal CdS–10% (GR–Ca) is much lower than both CdS–10% GR and CdS–30% GR. The PL intensity for the optimal CdS–10% (GR–Cu) is even lower than CdS–50% GR and CdS–70% GR. These results clearly suggest that the addition of a few amounts of metal ions can significantly optimize the charge carrier transfer pathway across the interface between CdS and GR and thus prolong the lifetime of photogenerated charge carriers, which consequently leads to the facts that (i) the negative shielding effect of a higher amount of GR can be counterbalanced effectively; and (ii) the photoactivity of CdS–GR is significantly improved. In addition, it should be noted that there is a moderate difference in the quenching degree of PL intensity among the samples CdS–10% (GR–Ca), CdS–10% (GR–Cr), CdS–10% (GR–Mn), CdS–30% (GR–Fe), CdS–30% (GR–Co), CdS–10% (GR–Ni), CdS–10% (GR–Cu), and CdS–30% (GR–Zn), which could mainly result from the difference of metal ion contents, the microscopic distribution of different metal ions in the interlayer matrix, and the intrinsic electronic property of different metal ions as interfacial mediator between CdS and the GR sheets.

In addition to the improved lifetime of charge carriers, the addition of metal ions is also able to promote the transfer efficiency of charge carriers across the interface between GR and semiconductor

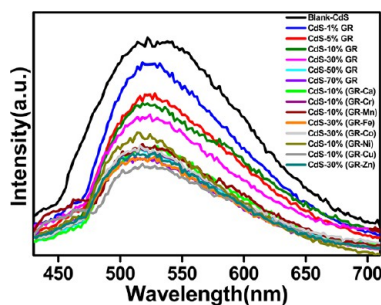


Figure 5. Photoluminescence (PL) spectra of blank CdS, CdS–GR, and CdS–(GR–M) ($M = \text{Ca}^{2+}$, Cr^{3+} , Mn^{2+} , Fe^{2+} , Co^{2+} , Ni^{2+} , Cu^{2+} , and Zn^{2+}) nanocomposites with different weight addition ratios of GR.

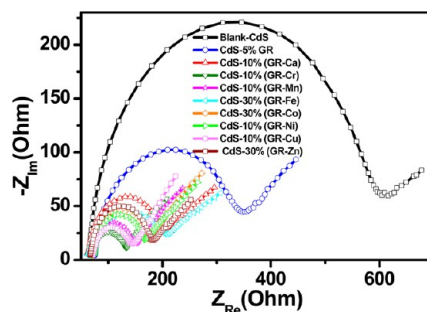


Figure 6. Electrochemical impedance spectroscopy (EIS) Nyquist diagrams of blank CdS, CdS–5% GR, and the optimal CdS–(GR–M) ($M = \text{Ca}^{2+}$, Cr^{3+} , Mn^{2+} , Fe^{2+} , Co^{2+} , Ni^{2+} , Cu^{2+} , and Zn^{2+}) nanocomposites in 0.5 M KCl aqueous solution containing 0.01 M $\text{K}_3[\text{Fe}(\text{CN})_6]/\text{K}_4[\text{Fe}(\text{CN})_6]$ (1:1).

CdS. To shed light on the charge carrier transport performance of the samples, electrochemical impedance spectroscopy (EIS), as a useful tool to characterize the charge carrier migration of the electrode materials,^{39,40} has been conducted for blank CdS, CdS–5% GR, and the optimal CdS–(GR–M) ($M = \text{Ca}^{2+}$, Cr^{3+} , Mn^{2+} , Fe^{2+} , Co^{2+} , Ni^{2+} , Cu^{2+} , and Zn^{2+}) electrodes. It can be seen from Figure 6 that the EIS Nyquist plots of all electrode materials give rise to semicircles at high frequencies, which corresponds to the charge transfer limiting process and is ascribed to the double-layer capacitance in parallel with the charge transfer resistance at the contact interface between electrode and electrolyte solution.^{39,40} As compared to blank CdS, the optimal CdS–(GR–M) ($M = \text{Ca}^{2+}$, Cr^{3+} , Mn^{2+} , Fe^{2+} , Co^{2+} , Ni^{2+} , Cu^{2+} , and Zn^{2+}) electrodes exhibit more depressed semicircles at high frequencies than does CdS–5% GR, indicating that the smaller resistance and more efficient transfer of charge carriers are obtained over the optimal CdS–(GR–M) ($M = \text{Ca}^{2+}$, Cr^{3+} , Mn^{2+} , Fe^{2+} , Co^{2+} , Ni^{2+} , Cu^{2+} , and Zn^{2+}) than those over CdS–5% GR. Besides, cyclic voltammetric technique has also been employed to study the photoelectrochemical properties of the photocatalysts. As displayed in Figure S24 (Supporting Information), the cyclic

voltammograms of blank CdS, CdS–5% GR, and the optimal CdS–(GR–M) ($M = \text{Ca}^{2+}, \text{Cr}^{3+}, \text{Mn}^{2+}, \text{Fe}^{2+}, \text{Co}^{2+}, \text{Ni}^{2+}, \text{Cu}^{2+}, \text{and Zn}^{2+}$) electrodes show two reversible anodic and cathodic peaks corresponding to the one-electron redox process.^{41–43} The current density obtained over the optimal CdS–(GR–M) electrodes is larger than that over CdS–5% GR and blank CdS. This implies that the introduction of a small amount of metal ions into the interlayer matrix of CdS and GR can improve the electron transfer across the contact interface between electrode and electrolyte solution.^{41–43} Among the optimal CdS–(GR–M) ($M = \text{Ca}^{2+}, \text{Cr}^{3+}, \text{Mn}^{2+}, \text{Fe}^{2+}, \text{Co}^{2+}, \text{Ni}^{2+}, \text{Cu}^{2+}, \text{and Zn}^{2+}$) samples, the modestly different degree in enhancing the transfer of charge carriers could be primarily explained by the difference in the contents, microscopic distribution, and intrinsic electronic property of the metal ions as interfacial mediator between GR and semiconductor CdS.

The surface area and porosity analysis has also been performed for the optimal CdS–(GR–M) and CdS–5% GR nanocomposites. It can be seen from Figure S25 and Table S4 (Supporting Information) that the Brunauer–Emmett–Teller (BET) surface areas and pore structure of the optimal CdS–10% (GR–M) ($M = \text{Ca}^{2+}, \text{Cr}^{3+}, \text{Mn}^{2+}, \text{Ni}^{2+}, \text{and Cu}^{2+}$) are similar to those of CdS–5% GR, indicating that the significantly enhanced photoactivity of the CdS–(GR–M) is not attributed to the difference of surface area and porosity among these samples but is primarily determined by the more efficient separation and transfer of photogenerated electron–hole pairs resulting from the introduction of a few amounts of metal ions as interfacial mediator between GR and CdS as discussed above. For the optimal CdS–30% (GR–M) ($M = \text{Fe}^{2+}, \text{Co}^{2+}, \text{and Zn}^{2+}$), the surface area and porosity volume are both moderately higher than CdS–5% GR, which can be attributed to the higher weight addition ratio of GR. However, the higher surface area and porosity volume are not likely responsible for the remarkably enhanced photoactivity because, for CdS–(GR–M) with higher weight addition ratios of GR (e.g., 50 and 70% GR), they have the higher surface area and porosity volume, but their photoactivity is much lower. This case is similar to that for CdS–GR photocatalysts, for which CdS–GR with higher weight addition ratio of GR has higher surface area and porosity volume but the photoactivity is decreased.^{3,18} Therefore, the difference in surface area and porosity cannot be the primary factor accounting for the significant photoactivity enhancement of the optimal CdS–(GR–M) as compared to CdS–GR.

Furthermore, we have also investigated the photocatalytic stability of optimal CdS–(GR–M) samples. As shown in Figures S26–S33 (Supporting Information), during four successive recycle times, no apparent activity loss was observed for both aerobic selective oxidation of benzyl alcohol

and anaerobic selective reduction of 4-nitroaniline (4-NA) over the optimal CdS–(GR–M) nanocomposites, indicating that CdS–(GR–M) composites are able to serve as stable photocatalysts under visible light irradiation. A series of controlled experiments with addition of different radical scavengers (Figure S34, Supporting Information) indicate that, for photocatalytic oxidation of benzyl alcohol over blank CdS, CdS–5% GR, and the optimal CdS–(GR–M) ($M = \text{Ca}^{2+}, \text{Cr}^{3+}, \text{Mn}^{2+}, \text{Fe}^{2+}, \text{Co}^{2+}, \text{Ni}^{2+}, \text{Cu}^{2+}, \text{and Zn}^{2+}$), the primary active radical species are photogenerated holes, electrons, and activated oxygen (e.g., $\text{O}_2^{\bullet-}$, whose presence is confirmed by the electron spin resonance (ESR) spectra analysis in Figure S35). Regarding photocatalytic selective reduction of 4-NA over blank CdS, CdS–5% GR, and optimal CdS–(GR–M), the reaction is driven by the photoexcited electrons, as revealed by the fact that the addition of electron scavenger $\text{K}_2\text{S}_2\text{O}_8$ into the reaction system completely terminates the reaction under visible light irradiation. These results also suggest that the introduction of metal ions into the interfacial layer between CdS and GR plays a negligible role on the underlying mechanism for photocatalytic oxidation of benzyl alcohol and reduction of 4-nitroaniline. The key role of metal ions is to act as “interfacial mediator” to optimize the transfer pathway of photogenerated charge carriers and improve their lifetime and transfer efficiency across the interface in the composite photocatalysts.

CONCLUSIONS

In summary, we for the first time have demonstrated a simple and general approach to significantly improve the photoactivity of GR–semiconductor nanocomposites *via* introducing a tiny amount of metal ions ($M = \text{Ca}^{2+}, \text{Cr}^{3+}, \text{Mn}^{2+}, \text{Fe}^{2+}, \text{Co}^{2+}, \text{Ni}^{2+}, \text{Cu}^{2+}, \text{and Zn}^{2+}$) into the interfacial layer matrix between the GR sheets and semiconductor CdS. Such interfacial composition engineering not only optimizes the photogenerated charge carrier transfer pathway across the interface between GR and semiconductor and efficiently improves the lifetime/transfer of charge carriers in the GR–semiconductor systems but also partially offsets the shielding effect of a greater addition of GR. Although we now cannot delineate each detail on how the metal ions as “interfacial mediator” optimize the atomic charge carriers pathway, our current results highlight that the more efficient and rational harness of electron conductivity of GR is not just a simple issue of tighter interfacial connection between the semiconductor and GR sheet. The optimization of interfacial composition between GR and semiconductor could offer a new opportunity to make GR fully play its role in accepting/transporting photogenerated electrons from semiconductor, by which the more efficient and smarter GR–semiconductor photocatalysts

would be achieved, instead of joining the GR-driven “gold rush”.⁶ Further effort and systematic work on

fabricating efficient GR–semiconductor composite photocatalysts along this line are in progress in our lab.

METHODS

Materials. Graphite powder, sulfuric acid (H₂SO₄), nitric acid (HNO₃), hydrochloric acid (HCl), potassium persulfate (K₂S₂O₈), phosphorus pentoxide (P₂O₅), potassium permanganate (KMnO₄), hydrogen peroxide, 30% (H₂O₂), calcium chloride (CaCl₂), chromium(III) chloride hexahydrate (CrCl₃·6H₂O), manganese(II) chloride tetrahydrate (MnCl₂·4H₂O), iron(II) chloride tetrahydrate (FeCl₂·4H₂O), cobalt(II) chloride hexahydrate (CoCl₂·6H₂O), nickel(II) chloride hexahydrate (NiCl₂·6H₂O), copper(II) chloride dihydrate (CuCl₂·2H₂O), zinc chloride (ZnCl₂), cadmium acetate (Cd(CH₃COO)₂·2H₂O), dimethyl sulfoxide (C₂H₆OS, DMSO), benzyl alcohol, 4-nitroaniline (C₆H₆N₂O₂), ammonium oxalate ((NH₄)₂C₂O₄, AO), benzoquinone (C₆H₄O₂, BQ) and tert-butyl alcohol (C₄H₁₀O, TBA) were obtained from Sinopharm Chemical Reagent Co., Ltd. (Shanghai, China). Benzotrifluoride (C₇H₅F₃, BTF) was purchased from Alfa Aesar China (Tianjin, China). All materials were analytical grade and used as received without further treatment. Deionized water was supplied by local sources.

Catalyst Preparation. *Fabrication of Graphene Oxide (GO).* Graphene oxide (GO) was fabricated by a modified Hummers method that involves a strong oxidation and exfoliation process of natural graphite powder in a liquid phase.³³ The details of the typical process is referenced in previous reports.^{2,4,26–28,30,34}

Preparation of GO–M (M = Ca²⁺, Cr³⁺, Mn²⁺, Fe²⁺, Co²⁺, Ni²⁺, Cu²⁺, and Zn²⁺). The precursor salts of Ca, Cr, Mn, Fe, Co, Ni, Cu, and Zn were dissolved in deionized water to produce the corresponding solution at a concentration of 10 mM. In the typical preparation process, a certain volume of the salt precursor solution was added to 200 mL of 0.5 mg·mL⁻¹ uniform-dispersed GO aqueous solution. Then, the above mixture was kept stirring for 2 h at room temperature. Afterward, the reaction mixture was centrifuged and washed with deionized water several times followed by drying at 60 °C. Then, the GO–M (M = Ca²⁺, Cr³⁺, Mn²⁺, Fe²⁺, Co²⁺, Ni²⁺, Cu²⁺, and Zn²⁺) was obtained.

Preparation of CdS–(GR–M) Composites. The preparation process is vividly delineated in Scheme 1. The given amount of the as-prepared GO–M was dispersed in 40 mL of DMSO by ultrasonication to obtain the homogeneous GO–M–DMSO dispersion into which 0.4 mmol Cd(CH₃COO)₂·2H₂O was added. The above mixture was stirred for 30 min and then transferred to a 50 mL Teflon-lined stainless steel autoclave to undergo a solvothermal treatment at 180 °C for 12 h. Afterward, the products were cooled to room temperature, separated by centrifugation, and then washed with acetone and absolute ethanol for three times and one time, respectively. After a drying process at 60 °C in an electric oven, a series of CdS–(GR–M) nanocomposites with different weight addition ratios of GR were obtained.

Preparation of CdS–GR and Blank CdS. For comparison purposes, CdS–GR was synthesized *via* the same solvothermal treatment as that of CdS–(GR–M) nanocomposites using GO instead of GO–M. Blank CdS was synthesized *via* the same solvothermal treatment in the absence of GO or GO–M.

Catalyst Characterization. Zeta-potentials (ζ) measurement in deionized water were determined by dynamic light scattering analysis (Zetasizer 3000HSA) at room temperature of 25 °C. X-ray photoelectron spectroscopy (XPS) measurement was carried out on a Thermo Scientific ESCA Lab250 spectrometer, which consists of monochromatic Al K α as the X-ray source, a hemispherical analyzer, and a sample stage with multiaxial adjustability, to obtain the surface composition of the sample. All of the binding energies were calibrated by the C1s peak at 284.6 eV. The Fourier transform infrared spectroscopy (FTIR) experiments were carried out on a Nicolet Nexus 670 FTIR spectrometer with a DTGS detector. The Raman spectra were recorded on a Renishaw inVia Laser Raman confocal microspectrometer with the laser at 532 nm. The phase composition of the samples was characterized by the powder X-ray diffractometer (XRD, Philip X' Pert Pro MPP) with

Ni-filtered Cu K α radiation ($\lambda = 1.5418 \text{ \AA}$) in the 2θ range from 10 to 80° with a scan rate of 0.02°/0.1 s. UV–vis diffuse reflectance spectroscopy (DRS) on a UV–vis spectrophotometer (PerkinElmer Lambda 950 UV–vis–NIR) was used to measure the optical properties of the samples with BaSO₄ as the internal reflectance standard. The morphology of the samples and the corresponding elemental mapping spectra were analyzed by transmission electron microscopy (TEM) using a JEOL model JEM 2010 EX instrument at an accelerating voltage of 200 kV. The photoluminescence (PL) spectra for solid samples were obtained on an Edinburgh Analytical Instrument FLS 920 spectrophotometer with the excitation wavelength of 358 nm. The electrochemical analysis was carried out in a conventional three-electrode cell using a Pt plate and a Ag/AgCl electrode as the counter electrode and reference electrode, respectively. The working electrode was prepared on fluorine-doped tin oxide (FTO) glass that was cleaned by sonication in ethanol for 30 min and dried at 80 °C. The boundary of FTO glass was protected using Scotch tape. The 5 mg sample was dispersed in 1 mL of *N,N*-dimethylformamide (DMF) by sonication to get a slurry. The slurry was spread onto the pretreated FTO glass. After air drying, the working electrode was further dried at 120 °C for 2 h to improve adhesion. Then, the Scotch tape was unstuck, and the uncoated part of the electrode was isolated with epoxy resin. The exposed area of the working electrode was 0.25 cm². The electrochemical impedance spectroscopy (EIS) experiments and cyclic voltammograms were conducted on a CHI 660D workstation (CH instrument, USA) in the electrolyte of 0.5 M KCl aqueous solution containing 0.01 M K₃[Fe(CN)₆]/K₄[Fe(CN)₆] (1:1) under open circuit potential conditions. Micromeritics ASAP2010 equipment was used to determine the nitrogen adsorption–desorption isotherms and the Brunauer–Emmett–Teller (BET) surface areas at 77 K. The sample was degassed at 140 °C for 5 h and then analyzed at 77 K. The relative pressure (P/P_0) range used for calculation of BET surface area was from 0.05 to 0.35. The radical species were analyzed by an electron spin resonance (ESR) spectrometer (Bruker EPR A300). In detail, the sample (5 mg) was dispersed in 0.5 mL of purified benzotrifluoride (BTF), into which 20 μ L of 5,5-dimethyl-1-pyrroline-*N*-oxide (DMPO)/benzyl alcohol solution (1:10, v/v) was added. The mixture was oscillated to obtain a well-blended suspension. The irradiation source ($\lambda > 420 \text{ nm}$) was a 300 W Xe arc lamp system, the very light source for our photocatalytic selective oxidation of alcohols. The parameters for the ESR spectrometer were as follows: center field = 3512 G, microwave frequency = 9.84 GHz, and power = 2.00 mW.

Catalyst Photoactivity. The photocatalytic selective oxidation of benzyl alcohol was performed as done in previous research.^{4,26–28,30,34,44–50} A mixture of benzyl alcohol (0.1 mmol) and 8 mg of photocatalyst was dispersed in the solvent of oxygen-saturated benzotrifluoride (BTF) (1.5 mL). The above mixture was transferred into a 10 mL Pyrex glass bottle filled with molecular oxygen at a pressure of 0.1 MPa and stirred for 30 min to make the catalyst blend evenly in the solution. The suspensions were irradiated by a 300 W Xe arc lamp (PLS-SXE 300, Beijing Perfect Light Co., Ltd.) with a UV-CUT filter to cut off light of wavelength <420 nm. After the reaction, the mixture was centrifuged at 12 000 rpm for 20 min to completely remove the catalyst particles. The remaining solution was analyzed with an Agilent gas chromatograph (GC-7820). The assignment of products was confirmed by a Hewlett-Packard gas chromatograph/mass spectrometer (HP-5973GC/MS). Conversion of benzyl alcohol, yield, and selectivity of benzaldehyde was defined as follows:

$$\begin{aligned} \text{conversion (\%)} &= [(C_0 - C_{BA})/C_0] \times 100 \\ \text{yield (\%)} &= C_{BAD}/C_0 \times 100 \\ \text{selectivity (\%)} &= [C_{BAD}/(C_0 - C_{BA})] \times 100 \end{aligned}$$

where C_0 is the initial concentration of benzyl alcohol, and C_{BA} and C_{BAD} are the concentration of the substrate benzyl alcohol and the benzaldehyde, respectively, at a certain time after the photocatalytic reaction.

The photocatalytic selective reduction of 4-nitroaniline (4-NA) to *p*-phenylenediamine (PPD) was performed in a self-designed photochemical reactor equipped with an electromagnetic stirrer.⁵¹ In a 100 mL glass flask equipped with a magnetic stir bar and a three-hole plug, 10 mg of catalyst was dispersed in 30 mL of a 20 mg·L⁻¹ aqueous solution of aromatic nitro compounds with 20 mg of ammonium oxalate (AO) as hole scavenger.^{52,53} The mixture was stirred in the dark for 1 h to ensure the establishment of adsorption–desorption equilibrium between the sample and reactant. Then, the above suspension was irradiated with a 300 W Xe arc lamp (PLS-SXE 300, Beijing Perfect Light Co., Ltd.) with a UV-CUT filter to cut off light of wavelength $\lambda < 420$ nm. During the process of the reaction, 3 mL of sample solution was taken from the reaction system at a certain time interval. Then, the solid photocatalyst was immediately separated from the mixed phase by centrifugation, and the remaining supernatant was analyzed on a Varian UV–vis spectrophotometer (Cary 50, Varian Co.). The whole experimental process was conducted under N₂ bubbling at the flow rate of 80 mL·min⁻¹. A Shimadzu high-performance liquid chromatograph (HPLC-LC20AT equipped with a C18 column and SPD-M20A photodiode array detector) was used to further investigate the assignment of products based on an external standard method. Conversion of 4-NA, yield and selectivity for the target product PPD were defined as follows:

$$\begin{aligned} \text{conversion (\%)} &= [(C_0 - C_r)/C_0] \times 100 \\ \text{yield (\%)} &= [(C_p/C_0) \times 100 \\ \text{selectivity (\%)} &= [C_p/(C_0 - C_r)] \times 100 \end{aligned}$$

where C_0 is the initial concentration of 4-NA, and C_r and C_p are the concentrations of reactant 4-NA and product PPD, respectively, at a certain time after the photocatalytic reaction.

Conflict of Interest: The authors declare no competing financial interest.

Acknowledgment. The support by the National Natural Science Foundation of China (NSFC) (21173045, 20903022, 20903023), the Award Program for Minjiang Scholar Professorship, the National Science Foundation (NSF) of Fujian Province for Distinguished Young Investigator Grant (2012J06003), Program for Returned High-Level Overseas Chinese Scholars of Fujian province, and the Project Sponsored by the Scientific Research Foundation for the Returned Overseas Chinese Scholars, State Education Ministry, is gratefully acknowledged.

Supporting Information Available: Additional characterization and photoactivity results. This material is available free of charge via the Internet at <http://pubs.acs.org>.

REFERENCES AND NOTES

- Iwase, A.; Ng, Y. H.; Ishiguro, Y.; Kudo, A.; Amal, R. Reduced Graphene Oxide as a Solid-State Electron Mediator in Z-Scheme Photocatalytic Water Splitting under Visible Light. *J. Am. Chem. Soc.* **2011**, *133*, 11054–11057.
- Zhang, Y.; Tang, Z.-R.; Fu, X.; Xu, Y.-J. TiO₂–Graphene Nanocomposites for Gas-Phase Photocatalytic Degradation of Volatile Aromatic Pollutant: Is TiO₂–Graphene Truly Different from Other TiO₂–Carbon Composite Materials? *ACS Nano* **2010**, *4*, 7303–7314.
- Li, Q.; Guo, B.; Yu, J.; Ran, J.; Zhang, B.; Yan, H.-J.; Gong, J. R. Highly Efficient Visible-Light-Driven Photocatalytic Hydrogen Production of CdS-Cluster-Decorated Graphene Nanosheets. *J. Am. Chem. Soc.* **2011**, *133*, 10878–10884.
- Zhang, Y.; Tang, Z.-R.; Fu, X.; Xu, Y.-J. Engineering the Unique 2D Mat of Graphene To Achieve Graphene–TiO₂ Nanocomposite for Photocatalytic Selective Transformation: What Advantage Does Graphene Have over Its Forebear Carbon Nanotube? *ACS Nano* **2011**, *5*, 7426–7435.
- Yang, M.-Q.; Xu, Y.-J. Selective Photoredox Using Graphene-Based Composite Photocatalysts. *Phys. Chem. Chem. Phys.* **2013**, *15*, 19102–19118.
- Zhang, N.; Zhang, Y.; Xu, Y.-J. Recent Progress on Graphene-Based Photocatalysts: Current Status and Future Perspectives. *Nanoscale* **2012**, *4*, 5792–5813.
- Xiang, Q.; Yu, J.; Jaroniec, M. Graphene-Based Semiconductor Photocatalysts. *Chem. Soc. Rev.* **2012**, *41*, 782–796.
- Kamat, P. V. Graphene-Based Nanoassemblies for Energy Conversion. *J. Phys. Chem. Lett.* **2011**, *2*, 242–251.
- Kamat, P. V. Graphene-Based Nanoarchitectures. Anchoring Semiconductor and Metal Nanoparticles on a Two-Dimensional Carbon Support. *J. Phys. Chem. Lett.* **2010**, *1*, 520–527.
- Huang, X.; Qi, X.; Boey, F.; Zhang, H. Graphene-Based Composites. *Chem. Soc. Rev.* **2012**, *41*, 666–686.
- Akhavan, O. Graphene Nanomesh by ZnO Nanorod Photocatalysts. *ACS Nano* **2010**, *4*, 4174–4180.
- Tu, W.; Zhou, Y.; Zou, Z. Versatile Graphene-Promoting Photocatalytic Performance of Semiconductors: Basic Principles, Synthesis, Solar Energy Conversion, and Environmental Applications. *Adv. Funct. Mater.* **2013**, *23*, 4996–5008.
- Mukherji, A.; Seger, B.; Lu, G. Q.; Wang, L. Nitrogen Doped Sr₂Ta₂O₇ Coupled with Graphene Sheets as Photocatalysts for Increased Photocatalytic Hydrogen Production. *ACS Nano* **2011**, *5*, 3483–3492.
- Zhang, H.; Lv, X.; Li, Y.; Wang, Y.; Li, J. P25-Graphene Composite as a High Performance Photocatalyst. *ACS Nano* **2010**, *4*, 380–386.
- Tu, W.; Zhou, Y.; Liu, Q.; Tian, Z.; Gao, J.; Chen, X.; Zhang, H.; Liu, J.; Zou, Z. Robust Hollow Spheres Consisting of Alternating Titania Nanosheets and Graphene Nanosheets with High Photocatalytic Activity for CO₂ Conversion into Renewable Fuels. *Adv. Funct. Mater.* **2012**, *22*, 1215–1221.
- Ng, Y. H.; Lightcap, I. V.; Goodwin, K.; Matsumura, M.; Kamat, P. V. To What Extent Do Graphene Scaffolds Improve the Photovoltaic and Photocatalytic Response of TiO₂ Nanostructured Films? *J. Phys. Chem. Lett.* **2010**, *1*, 2222–2227.
- Akhavan, O.; Ghaderi, E. Photocatalytic Reduction of Graphene Oxide Nanosheets on TiO₂ Thin Film for Photoinactivation of Bacteria in Solar Light Irradiation. *J. Phys. Chem. C* **2009**, *113*, 20214–20220.
- Xiang, Q.; Yu, J.; Jaroniec, M. Synergetic Effect of MoS₂ and Graphene as Cocatalysts for Enhanced Photocatalytic H₂ Production Activity of TiO₂ Nanoparticles. *J. Am. Chem. Soc.* **2012**, *134*, 6575–6578.
- Liang, Y. T.; Vijayan, B. K.; Gray, K. A.; Hersam, M. C. Minimizing Graphene Defects Enhances Titania Nanocomposite-Based Photocatalytic Reduction of CO₂ for Improved Solar Fuel Production. *Nano Lett.* **2011**, *11*, 2865–2870.
- Liang, Y. T.; Vijayan, B. K.; Lyandres, O.; Gray, K. A.; Hersam, M. C. Effect of Dimensionality on the Photocatalytic Behavior of Carbon–Titania Nanosheet Composites: Charge Transfer at Nanomaterial Interfaces. *J. Phys. Chem. Lett.* **2012**, *3*, 1760–1765.
- Du, J.; Lai, X.; Yang, N.; Zhai, J.; Kisailus, D.; Su, F.; Wang, D.; Jiang, L. Hierarchically Ordered Macro–Mesoporous TiO₂–Graphene Composite Films: Improved Mass Transfer, Reduced Charge Recombination, and Their Enhanced Photocatalytic Activities. *ACS Nano* **2011**, *5*, 590–596.
- Hayashi, H.; Lightcap, I. V.; Tsujimoto, M.; Takano, M.; Umeyama, T.; Kamat, P. V.; Imahori, H. Electron Transfer Cascade by Organic/Inorganic Ternary Composites of Porphyrin, Zinc Oxide Nanoparticles, and Reduced Graphene Oxide on a Tin Oxide Electrode That Exhibits Efficient Photocurrent Generation. *J. Am. Chem. Soc.* **2011**, *133*, 7684–7687.
- Lee, J. S.; You, K. H.; Park, C. B. Highly Photoactive, Low Bandgap TiO₂ Nanoparticles Wrapped by Graphene. *Adv. Mater.* **2012**, *24*, 1084–1088.
- Tu, W.; Zhou, Y.; Liu, Q.; Yan, S.; Bao, S.; Wang, X.; Xiao, M.; Zou, Z. An *In Situ* Simultaneous Reduction–Hydrolysis

- Technique for Fabrication of TiO₂-Graphene 2D Sandwich-like Hybrid Nanosheets: Graphene-Promoted Selectivity of Photocatalytic-Driven Hydrogenation and Coupling of CO₂ into Methane and Ethane. *Adv. Funct. Mater.* **2013**, *23*, 1743–1749.
25. Lightcap, I. V.; Kosel, T. H.; Kamat, P. V. Anchoring Semiconductor and Metal Nanoparticles on a Two-Dimensional Catalyst Mat. Storing and Shuttling Electrons with Reduced Graphene Oxide. *Nano Lett.* **2010**, *10*, 577–583.
 26. Zhang, N.; Zhang, Y.; Pan, X.; Fu, X.; Liu, S.; Xu, Y.-J. Assembly of CdS Nanoparticles on the Two-Dimensional Graphene Scaffold as Visible-Light-Driven Photocatalyst for Selective Organic Transformation under Ambient Conditions. *J. Phys. Chem. C* **2011**, *115*, 23501–23511.
 27. Zhang, N.; Zhang, Y.; Yang, M.-Q.; Tang, Z.-R.; Xu, Y.-J. A Critical and Benchmark Comparison on Graphene-, Carbon Nanotube-, and Fullerene-Semiconductor Nanocomposite as Visible Light Photocatalyst for Selective Oxidation. *J. Catal.* **2013**, *299*, 210–221.
 28. Yang, M.-Q.; Zhang, N.; Xu, Y.-J. Synthesis of Fullerene-, Carbon Nanotube- and Graphene-TiO₂ Nanocomposite Photocatalysts for Selective Oxidation. A Comparative Study. *ACS Appl. Mater. Interfaces* **2013**, *5*, 1156–1164.
 29. Ng, Y. H.; Iwase, A.; Kudo, A.; Amal, R. Reducing Graphene Oxide on a Visible-Light BiVO₄ Photocatalyst for an Enhanced Photoelectrochemical Water Splitting. *J. Phys. Chem. Lett.* **2010**, *1*, 2607–2612.
 30. Zhang, Y.; Zhang, N.; Tang, Z.-R.; Xu, Y.-J. Improving the Photocatalytic Performance of Graphene-TiO₂ Nanocomposite via a Combined Strategy of Decreasing Defects of Graphene and Increasing Interfacial Contact. *Phys. Chem. Chem. Phys.* **2012**, *14*, 9167–9175.
 31. Xiang, Q.; Yu, J.; Jaroniec, M. Preparation and Enhanced Visible-Light Photocatalytic H₂-Production Activity of Graphene/C₃N₄ Composites. *J. Phys. Chem. C* **2011**, *115*, 7355–7363.
 32. Fan, W.; Lai, Q.; Zhang, Q.; Wang, Y. Nanocomposites of TiO₂ and Reduced Graphene Oxide as Efficient Photocatalysts for Hydrogen Evolution. *J. Phys. Chem. C* **2011**, *115*, 10694–10701.
 33. Hummers, W. S.; Offeman, R. E. Preparation of Graphitic Oxide. *J. Am. Chem. Soc.* **1958**, *80*, 1339–1339.
 34. Zhang, Y.; Zhang, N.; Tang, Z.-R.; Xu, Y.-J. Graphene Transforms Wide Band Gap ZnS to a Visible Light Photocatalyst. The New Role of Graphene as a Macromolecular Photosensitizer. *ACS Nano* **2012**, *6*, 9777–9789.
 35. Cao, A.; Liu, Z.; Chu, S.; Wu, M.; Ye, Z.; Cai, Z.; Chang, Y.; Wang, S.; Gong, Q.; Liu, Y. A Facile One-Step Method To Produce Graphene-CdS Quantum Dot Nanocomposites as Promising Optoelectronic Materials. *Adv. Mater.* **2010**, *22*, 103–106.
 36. Liang, H.-W.; Liu, J.-W.; Qian, H.-S.; Yu, S.-H. Multiplex Templating Process in One-Dimensional Nanoscale: Controllable Synthesis, Macroscopic Assemblies, and Applications. *Acc. Chem. Res.* **2013**, *46*, 1450–1461.
 37. Wen, F.; Li, C. Hybrid Artificial Photosynthetic Systems Comprising Semiconductors as Light Harvesters and Biomimetic Complexes as Molecular Cocatalysts. *Acc. Chem. Res.* **2013**, *46*, 2355–2364.
 38. Xu, Y.-J.; Zhuang, Y.; Fu, X. New Insight for Enhanced Photocatalytic Activity of TiO₂ by Doping Carbon Nanotubes: A Case Study on Degradation of Benzene and Methyl Orange. *J. Phys. Chem. C* **2010**, *114*, 2669–2676.
 39. Guo, H.-L.; Wang, X.-F.; Qian, Q.-Y.; Wang, F.-B.; Xia, X.-H. A Green Approach to the Synthesis of Graphene Nanosheets. *ACS Nano* **2009**, *3*, 2653–2659.
 40. Lu, T.; Zhang, Y.; Li, H.; Pan, L.; Li, Y.; Sun, Z. Electrochemical Behaviors of Graphene-ZnO and Graphene-SnO₂ Composite Films for Supercapacitors. *Electrochim. Acta* **2010**, *55*, 4170–4173.
 41. Pan, X.; Zhao, Y.; Liu, S.; Korzeniewski, C. L.; Wang, S.; Fan, Z. Comparing Graphene-TiO₂ Nanowire and Graphene-TiO₂ Nanoparticle Composite Photocatalysts. *ACS Appl. Mater. Interfaces* **2012**, *4*, 3944–3950.
 42. Chatchai, P.; Murakami, Y.; Kishioka, S.-Y.; Nosaka, A. Y.; Nosaka, Y. Efficient Photocatalytic Activity of Water Oxidation over WO₃/BiVO₄ Composite under Visible Light Irradiation. *Electrochim. Acta* **2009**, *54*, 1147–1152.
 43. Ni, Y.; Cao, X.; Hu, G.; Yang, Z.; Wei, X.; Chen, Y.; Xu, J. Preparation, Conversion, and Comparison of the Photocatalytic and Electrochemical Properties of ZnS(en)_{0.5}, ZnS, and ZnO. *Cryst. Growth Des.* **2007**, *7*, 280–285.
 44. Zhang, M.; Chen, C.; Ma, W.; Zhao, J. Visible-Light-Induced Aerobic Oxidation of Alcohols in a Coupled Photocatalytic System of Dye-Sensitized TiO₂ and TEMPO. *Angew. Chem., Int. Ed.* **2008**, *47*, 9730–9733.
 45. Zhang, M.; Wang, Q.; Chen, C.; Zang, L.; Ma, W.; Zhao, J. Oxygen Atom Transfer in the Photocatalytic Oxidation of Alcohols by TiO₂: Oxygen Isotope Studies. *Angew. Chem., Int. Ed.* **2009**, *48*, 6081–6084.
 46. Pan, X.; Zhang, N.; Fu, X.; Xu, Y.-J. Selective Oxidation of Benzyl Alcohol over TiO₂ Nanosheets with Exposed {001} Facets: Catalyst Deactivation and Regeneration. *Appl. Catal., A* **2013**, *453*, 181–187.
 47. Zhang, N.; Zhang, Y.; Pan, X.; Yang, M.-Q.; Xu, Y.-J. Constructing Ternary CdS-Graphene-TiO₂ Hybrids on the Flatland of Graphene Oxide with Enhanced Visible Light Photoactivity for Selective Transformation. *J. Phys. Chem. C* **2012**, *116*, 18023–18031.
 48. Tang, Z.-R.; Zhang, Y.; Xu, Y.-J. Tuning the Optical Property and Photocatalytic Performance of Titanate Nanotube toward Selective Oxidation of Alcohols under Ambient Conditions. *ACS Appl. Mater. Interfaces* **2012**, *4*, 1512–1520.
 49. Liu, S.; Zhang, N.; Tang, Z.-R.; Xu, Y.-J. Synthesis of One-Dimensional CdS@TiO₂ Core-Shell Nanocomposites Photocatalyst for Selective Redox: The Dual Role of TiO₂ Shell. *ACS Appl. Mater. Interfaces* **2012**, *4*, 6378–6385.
 50. Zhang, N.; Fu, X.; Xu, Y.-J. A Facile and Green Approach to Synthesize Pt@CeO₂ Nanocomposite with Tunable Core-Shell and Yolk-Shell Structure and Its Application as a Visible Light Photocatalyst. *J. Mater. Chem.* **2011**, *21*, 8152–8158.
 51. Zhang, N.; Xu, Y.-J. Aggregation- and Leaching-Resistant, Reusable and Multifunctional Pd@CeO₂ as a Robust Nanocatalyst Achieved by a Hollow Core-Shell Strategy. *Chem. Mater.* **2013**, *25*, 1979–1988.
 52. Zhang, Y.; Zhang, N.; Tang, Z.-R.; Xu, Y.-J. Transforming CdS to an Efficient Visible Light Photocatalyst for Selective Oxidation of Saturated Primary C-H Bonds under Ambient Conditions. *Chem. Sci.* **2012**, *3*, 2812–2822.
 53. Carp, O.; Huisman, C. L.; Reller, A. Photoinduced Reactivity of Titanium Dioxide. *Prog. Solid State Chem.* **2004**, *32*, 33–177.